ADVANCED ENERGY MATERIALS

www.advenergymat.de

# Fractal $(Ni_xCo_{1-x})_9Se_8$ Nanodendrite Arrays with Highly Exposed $(01\overline{1})$ Surface for Wearable, All-Solid-State Supercapacitor

*Peiyu Yang, Zeyi Wu, Yingchang Jiang, Zhichang Pan, Wenchao Tian, Le Jiang, and Linfeng Hu**

**Hierarchical nanostructures with highly exposed active surfaces for high-performance pseudocapacitors have attracted considerable attention. Herein, a one-step growth of $(Ni_xCo_{1-x})_9Se_8$ solid solution series in various conductive substrates as advanced electrodes for flexible, foldable supercapacitors is developed. The formation of $(Ni_xCo_{1-x})_9Se_8$ solid solution is confirmed by Vegard's law. Interestingly, the as-grown $(Ni_xCo_{1-x})_9Se_8$ solid solution series spontaneously crystallized into nanodendrite arrays with hierarchical morphology and fractal feature. The optimized $(Ni_{0.1}Co_{0.9})_9Se_8$ nanodendrites deliver a specific capacitance of 3762 F $g^{-1}$ at a current density of 5 A $g^{-1}$ and remains 94.8% of the initial capacitance after 5000 cycles, owing to the advantage from fractal feature with numerous exposed $(01\overline{1})$ surface as well as fast ion diffusion. The as-assembled flexible $(Ni_{0.1}Co_{0.9})_9Se_8$@carbon fiber cloth (CFC)//PVA/KOH//reduced graphene oxide@CFC device exhibits an ultrahigh energy density of 17.0 Wh $kg^{-1}$@3.1 kW $kg^{-1}$, outperforming recently reported pseudocapacitors based on nickel-cobalt sulfide and selenide counterparts. This study provides rational guidance toward the design of fractal feature with superior electrochemical performances due to the significantly increased electrochemical active sites. The resulting device can be easily folded, pulled, and twisted, enabling potential applications in high-performance wearable and gadget devices.**

The development of high-efficiency energy storage devices for an ever-growing demand of high energy density to power electric vehicles and various flexible electronics has attracted widespread interests.[1–5] Supercapacitors have been receiving considerable attention due to their high power density and fast charging rate.[6] However, the main challenge for practical application of supercapacitors is their low energy density.[7] Recent experimental and theory progresses on electrochemical energy storage have revealed three emerging strategies for high energy density devices: (1) The development of novel active materials with high intrinsic conductivity and electrochemical activity. Typically, compared with metal oxides and chalcogenides, metal selenides generally show superior electrochemical properties owing to the lower bandgap and higher electronic conductivity.[8–12] (2) The optimal utilization of the synergistic effect of two different metal elements to increase electrochemical surface active sites.[13,14] Liu et al. reported that surface active sites in Ni—Co bimetallic hydroxides is tunable through various Ni/Co composition ratios, and the enhancement in the electroactive sites participated in the redox reaction due to possible valence interchange or charge hopping between Co and Ni cations.[15] (3) The in situ growth of active nanomaterials with high active sites on various conductive current collectors to improve the interfacial contact. In this case, the satisfactory electrical conductivity at the active material/current collector interface due to the absence of any insulating polymer binder significantly facilitates the electron transport and enhance the energy density.[16,17] Attempts to combine the aforementioned emerging strategies together, the realization of in situ growth of Ni—Co—Se compounds on various current collectors should be very promising as advanced electrode for high energy density devices. Recent study also confirms the advance in such Ni—Co—Se systems.[18–20] However, all approaches in the previous reports generally ask for complicated two-step procedures including the secondary ion-exchange or selenization process, which leads to difficulties on the in situ growth on conductive substrates. Undoubtedly, the development of rapid in situ synthesis of ternary Ni—Co—Se nanostructures on various current collectors is highly desired.

On the other hand, fractal structures generally provide a maximized exposed surface and highly efficient transport for substance, thus have attracted considerable interest for their appealing applications in solar cells and biosensors.[21] For example, recent research has proved that silicon fractal arrays can greatly improve the detection sensitivity of rare cancer cells in whole blood by enhancing topographic interactions.[22] However, up to date the rational design of fractal structures

---

P. Y. Yang, Z. Y. Wu, Dr. Y. C. Jiang, Z. C. Pan, W. C. Tian,
L. Jiang, Prof. L. F. Hu
Department of Materials Science
Fudan University
Shanghai 200433, P. R. China
E-mail: linfenghu@fudan.edu.cn

The ORCID identification number(s) for the author(s) of this article can be found under https://doi.org/10.1002/aenm.201801392.

**DOI: 10.1002/aenm.201801392**

for electrochemical energy storage devices has still been rarely reported.

Inspired by these considerations, herein, we developed a one-step growth of $(Ni_xCo_{1-x})_9Se_8$ solid-solution series in various conductive substrates as advanced electrodes for flexible, asymmetric supercapacitors. Interestingly, the as-grown $(Ni_xCo_{1-x})_9Se_8$ solid solution series spontaneously crystallized into nanodendrite arrays on nickel foam (NF) and carbon fiber cloth (CFC) surface with hierarchical morphology and fractal feature. The optimal $(Ni_{0.1}Co_{0.9})_9Se_8$ nanodendrites on NF deliver a specific capacitance of 3762 F $g^{-1}$ at a current density of 5 A $g^{-1}$ and remains 94.8% of its initial capacitance after 5000 cycles, owing to the advantage from fractal feature with numerous exposed $(01\bar{1})$ surface as well as fast ion diffusion. The resulting solid-state supercapacitor can be easily folded, pulled, and twisted, showing potential application on high-performance wearable and gadget devices.

Our synthetic method of $(Ni_xCo_{1-x})_9Se_8$ $(0 < x < 1)$ solid solutions is almost similar to Xie's method with minor modification.[23] The characteristic X-ray diffraction (XRD) patterns of the products with different Ni/Co ratios are shown in **Figure 1**a. At $x = 0$, the pattern matches well with the standard pattern of cubic $Co_9Se_8$ (JCPDS Card No. 09-0233), and the six prominent peaks can be indexed to the scattering from (311), (222), (400), (511), (440), and (622) planes, respectively. The products with $0 < x \leq 0.2$ generally show the similar XRD patterns with that of $x = 0$. Note that two impurity peaks at about 37° and 42° (indexed to an intermediate phase of hexagonal CoSe, JCPDS Card No. 15-0464) start to occur as the Ni mole fraction up to 0.3, indicating that the upper limit for the formation of $(Ni_xCo_{1-x})_9Se_8$ solid solutions should be less than $x = 0.3$. With further increase in Ni dopant concentration, a mixture of cubic and hexagonal phases is identified, suggesting structure transition from cubic to hexagonal phase takes place at higher $x$ values.[24] While at $x = 1.0$, the peaks fit well with pure NiSe phase (JCPDS Card No. 02-0892) with a hexagonal crystal structure as depicted in Figure 1e. As shown in Figure 1b, the diffraction peaks of (222) plane of the products systematically shift toward smaller angles along with the increase of Ni content from 0.01 to 0.20. Also, the (222) diffraction peak presents a

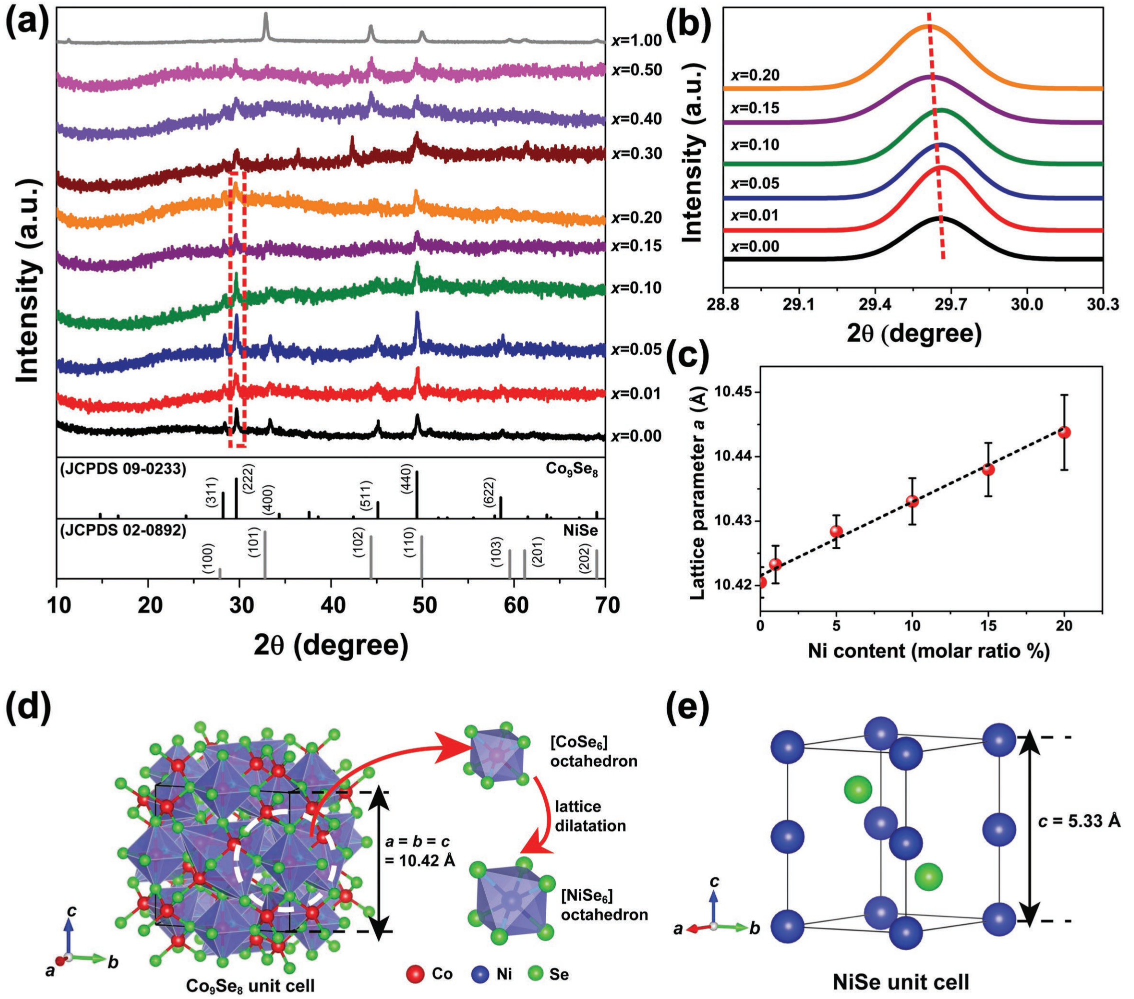

**Figure 1.** a) XRD patterns of $(Ni_xCo_{1-x})_9Se_8$ solid solutions with various Ni doping. JCPDS 02-0892 (for NiSe phase) and 09-0233 (for $Co_9Se_8$ phase) patterns are shown for comparison (vertical lines). b) The XRD peaks of the (222) plane of $(Ni_xCo_{1-x})_9Se_8$ solid solutions for various values of $x$. c) The lattice parameter of $(Ni_xCo_{1-x})_9Se_8$ solid solutions as a function of Ni molar fraction. d) The schematic illustration of the formation of $(Ni_xCo_{1-x})_9Se_8$ solid solution. e) The unit cell of NiSe crystal.

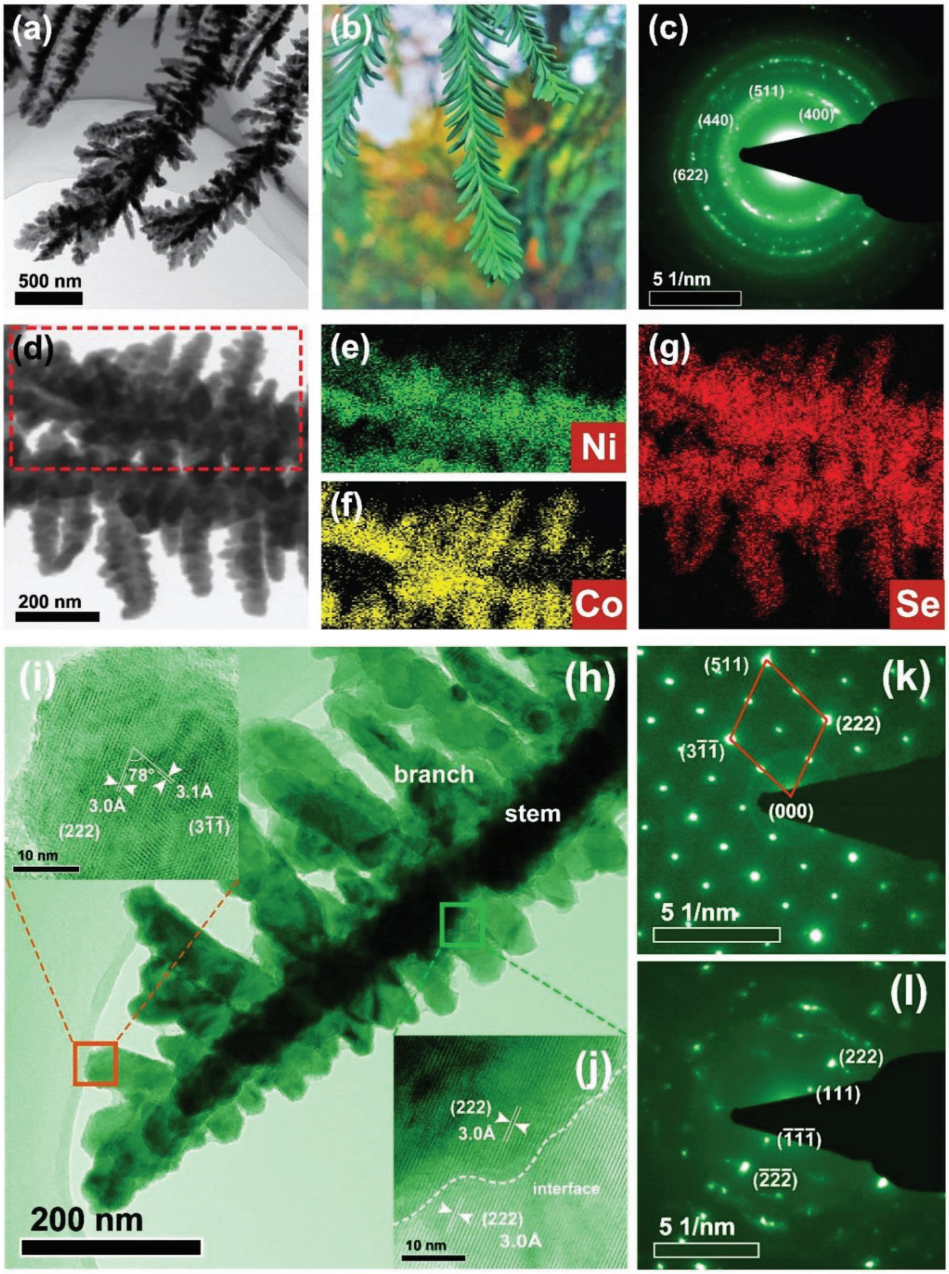

**Figure 2.** a) Typical TEM image of several hierarchical $(Ni_xCo_{1-x})_9Se_8$ nanodendrite ($x = 0.1$). b) A photograph of the hierarchical structure in the branches of pine tree. c) The corresponding SAED pattern of several $(Ni_xCo_{1-x})_9Se_8$ nanodendrites ($x = 0.1$). d–g) EDS mapping with uniform distribution of Ni, Co, and Se elements. Typical HRTEM image of h) an individual $(Ni_xCo_{1-x})_9Se_8$ nanodendrite ($x = 0.1$), i) the branch, and j) the branch/stem interface. The corresponding SAED patterns taken from the k) branch side and l) stem/branch interface, respectively.

well-defined shape with symmetric feature. Moreover, the lattice parameter *a* calculated from XRD data of the $(Ni_xCo_{1-x})_9Se_8$ samples increases from 10.42 to 10.44 Å, which is in agreement with the successive shift of the (222) peak in **Figure 2**b. This linear trend well follows the Vegard's law,[25] providing essential evidence that $Ni^{2+}$ and $Co^{2+}$ are successfully incorporated into the cubic lattice to form homogeneous $(Ni_xCo_{1-x})_9Se_8$ solid solutions.[26] Considering the very close ionic radii of $Ni^{2+}$ (0.83Å) and $Co^{2+}$ (0.79 Å), Ni dopant may substitute for the Co atoms in the central position of $[CoSe_6]$ octahedron in the solid solution crystal. The lattice parameter expands in Figure 1c should be attributed to the slightly larger ion radii of $Ni^{2+}$ (0.83Å) than $Co^{2+}$ (0.79 Å).[27] The elemental composition of the $(Ni_xCo_{1-x})_9Se_8$ ($x = 0.1$) solid solution sample is further characterized by the X-ray photoelectron spectroscopy (XPS) as shown in Figure S1 (Supporting Information). The peaks of Ni 2p (Figure S1b, Supporting Information) can be identified to the $2p_{1/2}$, $2p_{3/2}$ and their satellite peaks of $Ni^{2+}$; also, the $2p_{1/2}$, $2p_{3/2}$ peaks of the Ni-Se can be found at 870.40 and 853.2 eV,[28] further demonstrating the Ni has been successfully doped into the $(Ni_xCo_{1-x})_9Se_8$ ($x = 0.1$) solid solution crystal to form Ni—Se bonding. The Co 2p spectra include two pairs of $2p_{1/2}$, $2p_{3/2}$ peaks and their satellite peaks of $Co^{2+}$; and a Co—Se peak located at 778.7 eV is spotted as well in Figure S1c (Supporting Information).[28,29] Two pairs of $3d_{3/2}$, $3d_{5/2}$ peaks assigned to Ni—Se and Co—Se can be detected in Figure S1d (Supporting Information), respectively.[30,31]

The in situ growth of $(Ni_xCo_{1-x})_9Se_8$ nanodendrite arrays on NF surface can be realized by placing a clean piece of NF into the Teflon autoclave. The color of NF turn from initially gray to black accompanied by the in situ growing. The morphology of the as-prepared samples is characterized by scanning electron microscopy (SEM) observation. As shown in Figure S2 (Supporting Information), with tunable Ni/Co ratios, all $(Ni_xCo_{1-x})_9Se_8$ samples ($x$ = 0.00, 0.05, 0.10, 0.15, 1.00) show a high coverage of numerous nanodendrite arrays on the surface of NF. From the enlarged SEM images in Figure S2 (Supporting Information), all samples other than pure NiSe@NF sample exhibit a unique hierarchical morphology and fractal feature composing of numerous nanobranches and nanostems. Figure 2a further depicts the transmission electron microscopy (TEM) observation of the as-grown hierarchical $(Ni_xCo_{1-x})_9Se_8$ ($x$ = 0.10) nanodendrite on NF surface. Such a microscopic morphology shows great similarity with the branches of pine tree in macroscopic world (Figure 2b). The selected area electron diffraction (SAED) pattern of several nanodendrites (Figure 2c) presents a series of diffraction rings. The solid solution formation of $(Ni_{0.1}Co_{0.9})_9Se_8$ is further supported by the energy dispersive spectroscopy (EDS) mapping under TEM observation (Figure 2d–g). The Ni, Co, and Se elements are uniformly distributed through an individual $(Ni_{0.1}Co_{0.9})_9Se_8$ nanodendrite. Note that the signal of all elements detected from the branch position is much fainter than that from the stem area, implying the thickness of stem area is larger than that of at the branch area. Furthermore, the Ni element displays slightly weaker signal compared with signal of Co and Se elements, which is well agreement with the small amount of Ni doping.

A high-magnification transmission electron microscopy (HRTEM) image of $(Ni_xCo_{1-x})_9Se_8$ nanodendrite ($x$ = 0.1) is shown in Figure 2h, revealing that many nanorod-like branches rooted in central stem of the hierarchical structure.[32] Seen from the tip of this nanodendrite, the diameter of the $(Ni_{0.1}Co_{0.9})_9Se_8$ stem is estimated to be ≈50–100 nm and their length ranges from 1 to 5 µm, with nanobranches about 100–600 nm in length. The clear lattice fringes shown in Figure 2i from the branch area exhibit interplanar spacings of 3.0 and 3.1 Å, which can be assigned to (222) and $(3\bar{1}\bar{1})$ planes of $(Ni_xCo_{1-x})_9Se_8$, respectively. The HRTEM image in Figure 2j clearly shows the interface between branch area and the stem. Note that the lattice fringe of (222) plane is successive at this interface, indicating the branch area was epitaxially grown on the stem of a hierarchical $(Ni_xCo_{1-x})_9Se_8$ nanodendrite along [111] direction. The SAED pattern (Figure 2k) taken from the branch area shows bright diffraction spots with hexagonally arranged sharp diffraction spots which can be indexed to the $[01\bar{1}]$ zone axis pattern, demonstrating their single-crystalline nature with their highly exposed $(01\bar{1})$ surface. The SAED pattern taken from the branch/stem interface is given in Figure 2l. The diffraction spots of (222) plane can also be detected. However, some polycrystalline rings with faint intensity in this pattern suggest possible orientation mismatching of small grains at the interface.

It is also noteworthy that the morphology of the as-synthesized $(Ni_xCo_{1-x})_9Se_8$ is quite different between the bottom of the autoclave and the surface of the Ni foam. A large number of 2D nanosheets with irregular shape can be found at the bottom of the autoclave (Figure S3a, Supporting Information), and the product in situ grown on the surface of the Ni foam substrate shows unique morphology of hierarchical nanodendrite arrays (Figure S3b, Supporting Information). We consider that the solid-state substrate should play a key role in the nucleation of our $(Ni_{0.1}Co_{0.9})_9Se_8$ nanodendrites. In general, the crystal grown on the surface of the solid-state substrate follows a heterogeneous nucleation pathway, leading to an anisotropic growth along an oriented crystal direction. Their growth mechanism could be similar to that of $Ag_2Se$, $PbMoO_4$ dendrites reported by other groups:[33–35] the $(Ni_{0.1}Co_{0.9})_9Se_8$ nanoparticles might be directly formed on the surface of the substrate, and then assembled to dendritic nanostructure via self-organization of adjacent nanoparticles, which is well-known as "oriented attachment process."

Considering the unique 3D hierarchical morphology with fractal feature, the as-grown $(Ni_xCo_{1-x})_9Se_8$ nanodendrite arrays are expected to have superior electrochemical properties. The electrochemical performance of $(Ni_xCo_{1-x})_9Se_8$@NF with various $x$ value are investigated using a three-electrode cell configuration in 1 M KOH as aqueous electrolyte and the Ag/AgCl electrode as reverence at ambient temperature. Generally, the accurate measurement of loading mass of the active material in the in situ growth process is very important to estimate the corresponding electrochemical properties. In the present study, this value was determined by subtracting the weight before and after the in situ growth, and this measurement was carried out three times to eliminate experimental errors. From the cyclic voltammetry (CV) curves at a scan rate of 2 mV $s^{-1}$ (**Figure 3**a), the integral area of $(Ni_xCo_{1-x})_9Se_8$@NF at $x = 0.10$ is much larger than the other samples. Coupled with the corresponding galvanostatic charge–discharge (GCD) measurements at a current density of 5 A $g^{-1}$ (Figure 3b), the discharging time of $(Ni_{0.1}Co_{0.9})_9Se_8$@NF is the longest as well. The specific capacitances calculated from the GCD curves displayed in Figure 3c are 1590, 1711, 2183, 3762, 2582, 2470, 2359, 1748, 1403, and 1062 F$g^{-1}$ as the Ni dopant is 0.00, 0.01, 0.05, 0.10, 0.15, 0.20, 0.30, 0.40, 0.50, and 1.00, respectively. As summarized in Figure 3c, the specific capacitances of $(Ni_xCo_{1-x})_9Se_8$@NF series increase sharply as the dopant Ni content increases until it reached the optimal content of 0.10. This significant increment should be attributed to the enhancement of the electroactive sites engaged in the redox reaction due to the charge transfer between Ni and Co cations, which is also observed in the previously reported Ni—Co binary hydroxide systems.[36]

The energy storage properties of the optimized $(Ni_{0.1}Co_{0.9})_9Se_8$@NF sample were studied in detail as shown in Figure S4 (Supporting Information). The CV curves at different scan rate reveal a pair of redox peaks at 0.25 and 0.36 V (2 mV $s^{-1}$ of scan rate) as a result of the synergistic effect between Ni and Co cations. Additionally, a behavior of redox peaks shifting accordingly toward higher and lower potential

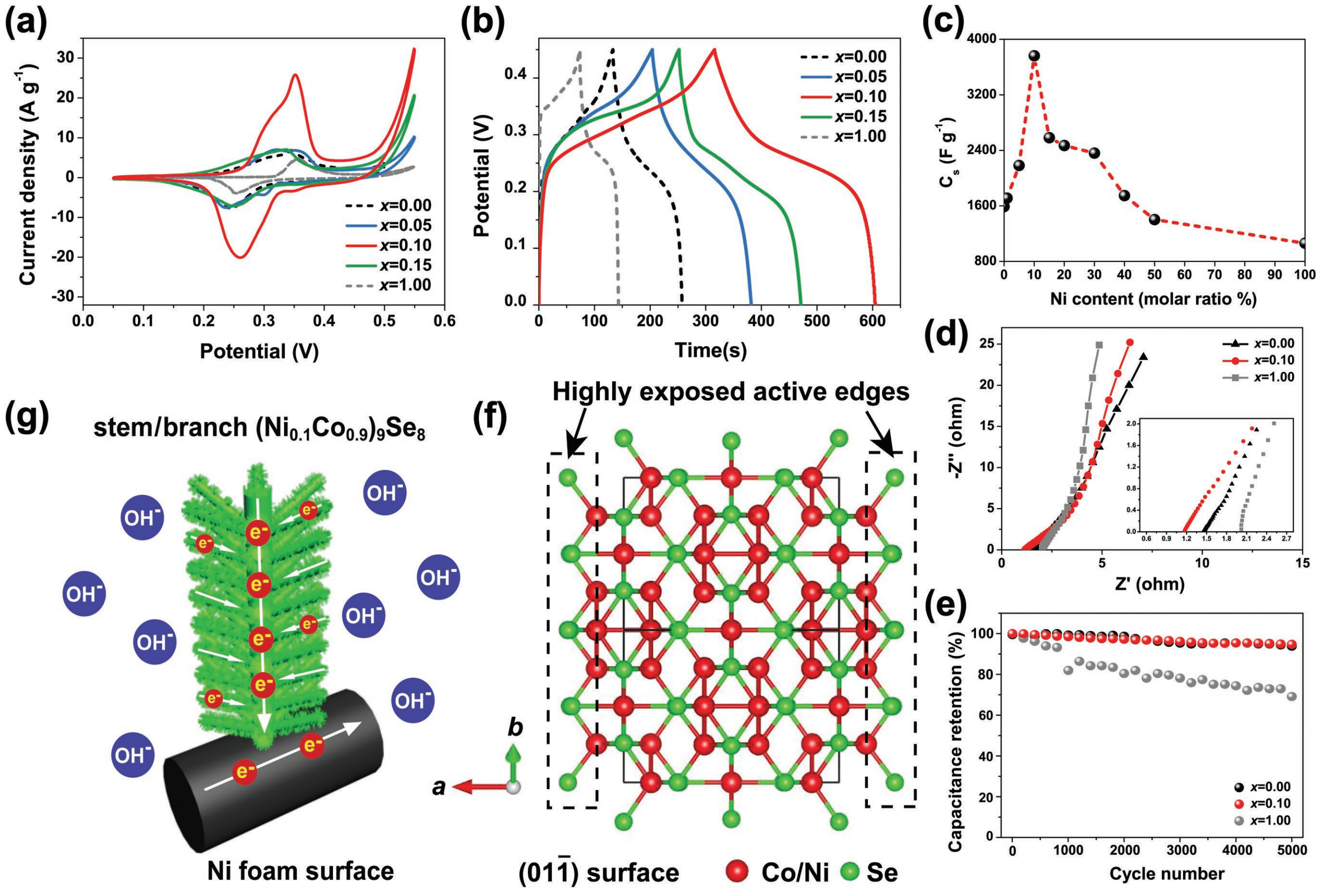

**Figure 3.** a) CV curves and b) GCD curves of $(Ni_xCo_{1-x})_9Se_8$@NF with different $x$ value using a three-electrode cell configuration. c) Specific capacitance calculated from the GCD data at different $x$ value. d) Nyquist plot of $Co_9Se_8$@NF, $(Ni_{0.1}Co_{0.9})_9Se_8$@NF, and NiSe@NF. e) Cycle performances of $Co_9Se_8$@NF, $(Ni_{0.1}Co_{0.9})_9Se_8$@NF, and NiSe@NF. f) The atomic configuration of the exposed $(01\bar{1})$ surface. g) Schematic diagram of the virtues of the interconnected stem-branch structure.

directions as scan rate increases from 2 to 30 mV $s^{-1}$ is observed with a well-retained CV curve (without any distortion in the shape), indicating the great reversibility of $(Ni_{0.1}Co_{0.9})_9Se_8$. The corresponding GCD curves with different current densities varying from 5 to 30 A $g^{-1}$, and the nonlinear charging/discharging curves further verify the faradaic reaction over the electroactive materials on the electrode. In comparison with the pure NiSe and $Co_9Se_8$ electrodes (Figure S5, Supporting Information), the voltage ($iR$) drop of the $(Ni_{0.1}Co_{0.9})_9Se_8$ electrode is significantly lower, implying a rather small equivalent series resistance exists which leads to the favorable power characteristic of supercapacitors.[37,38] The calculated specific capacitances at different current densities from 5, 10, 15, 20, 25, and 30 A $g^{-1}$ are 3762, 3673, 3598, 3547, 3504, and 3454 F $g^{-1}$, suggesting the satisfactory rate capability of the optimized $(Ni_{0.1}Co_{0.9})_9Se_8$@NF sample (Figure S6, Supporting Information).

The electrochemical impedance spectroscopy (EIS) is carried out to further gain in-depth knowledge of the reaction kinetics and electrical conductivity of as-obtained electrodes. From the Nyquist plot presented in Figure 3d, all $(Ni_xCo_{1-x})_9Se_8$@NF electrodes with $x = 0.0, 0.1, 1.0$ show an extremely small charge transfer resistance ($R_{ct}$) nearly negligible, suggesting the fast transportation of ions or charges at the interface between $(Ni_xCo_{1-x})_9Se_8$ nanodendrites and liquid electrolyte owing to the advantages of the dendritic nanostructure. More importantly, the equivalent series resistance ($R_s$) observed at a higher frequency region is clearly in the order that $(Ni_{0.1}Co_{0.9})_9Se_8$@NF < $Co_9Se_8$@NF < NiSe@NF, demonstrating the optimal doping in $(Ni_xCo_{1-x})_9Se_8$ solid solution series leads to the lowest $R_s$.[39] As depicted in Figure 3e, the optimized $(Ni_{0.1}Co_{0.9})_9Se_8$@NF electrode remains almost 94.8% of the initial capacitance after 5000 cycles at current density of 30 A $g^{-1}$, while its $(Ni_xCo_{1-x})_9Se_8$ counterparts ($x = 0.0, 1.0$) retain 93.8 and 69.2%, respectively. The corresponding TEM images of the $(Ni_{0.1}Co_{0.9})_9Se_8$ sample before and after 5000 cycles are shown in Figure S7 (Supporting Information). The dendritic nanostructure was well-maintained after 5000 cycles, demonstrating its long-term stability in morphology.

The remarkable electrochemical properties of the as-optimized $(Ni_{0.1}Co_{0.9})_9Se_8$@NF electrode should be ascribed to the following reasons: (1) The hierarchical morphology with fractal characteristic can provide maximum surface areas and numerous active edges. As evident by the TEM observation in Figure 2k, the $(01\bar{1})$ surface of $(Ni_xCo_{1-x})_9Se_8$ nanodendrites is highly exposed. The densely packed nanobranches in the hierarchical structure adequately fill the void spaces between the nanostems and increase the specific surface area, which further guarantee the efficient interfacial contact between liquid electrolyte and the electroactive bimetallic selenides. (2) The hierarchical stem/branch structure with homogeneous chemical distribution serves as an effective charge transport pathway. The charges provided from the numerous active sites in $(01\bar{1})$ surface would form a high-speed stream through the highly conducted "highway" then transport to the current collector, as schematically illustrated in Figure 3f,g.[40,41] (3) The one step in situ growth strategy ensures the bind-free structure and strong adherence of electroactive $(Ni_{0.1}Co_{0.9})_9Se_8$ on conductive substrates, which could significantly reduce the "dead volume" and improve the electrochemical activity of the electrode. The direct growth also reduces the interface resistance gap between the substrate and active compounds and acts as an electron superhighway to enhance the ion/electron transfer rate.[42] (4) The electrochemical signature for Ni and Co compounds in KOH electrolyte is usually closer to that of a "battery" material.[43–45] In general, the current obeys a power-law relationship with the sweep rate leading to[45]

$$i = aV^b \tag{1}$$

where *a* and *b* are adjustable values. Whereas a *b*-value of 0.5 would indicate that the current is controlled by semi-infinite linear diffusion, a value of 1 indicates that the current is surface-controlled. In our case, for sweep rates ranging from 2 to 5 mV $s^{-1}$, the *b*-value for both the cathodic and anodic peaks is 0.77 and 0.81, respectively. With increasing scan rates, the *b*-value decreased to 0.51 and 0.53 (Figure S8, Supporting Information). Thus, the charge stored by the battery-type mechanism increases and gradually dominates the total storage capacity at high scan rates. This result is consistent with that in $T$-$Nb_2O_5$ reported by Dunn and co-workers.[46] To further distinguish the relative contributions of battery-type mechanism and surface pseudocapacitive mechanism, the modified powers law presented below is used for calculation[47,48]

$$I_p = I_{surface} + I_{bulk} = C_{surface}V + C_{bulk}V^{1/2} \tag{2}$$

where $I_p$ is the peak current density; $V$ is the scan rate; $C_{surface}V$ and $C_{bulk}V^{1/2}$ are corresponding to the current contributions from the surface pseudocapacitive effect ($I_{surface}$) and bulk process ($I_{bulk}$), respectively.[48] Through determining the values of $C_{surface}$ and $C_{bulk}$, the respective contribution of current density from the surface pseudocapacitive and the battery-like bulk process at various scan rates can be identified in Figure S9 (Supporting Information).

All-solid-state asymmetric supercapacitors (ASC) with $(Ni_{0.1}Co_{0.9})_9Se_8$@NF as the positive electrode, reduced graphene oxide (rGO) as the negative electrode, and poly(vinyl alcohol) (PVA)–KOH gel as electrolyte were assembled subsequently (**Figure 4**). The CV and GCD curves of the negative rGO electrode are shown in Figure S10 (Supporting Information). The mass ratio of the two opposite electrodes is based on the charge balancing relation. As seen in Figure 4b, the rGO@NF properly fills up the voltage window of −0.1 to 0 V, hence widens the working potential window

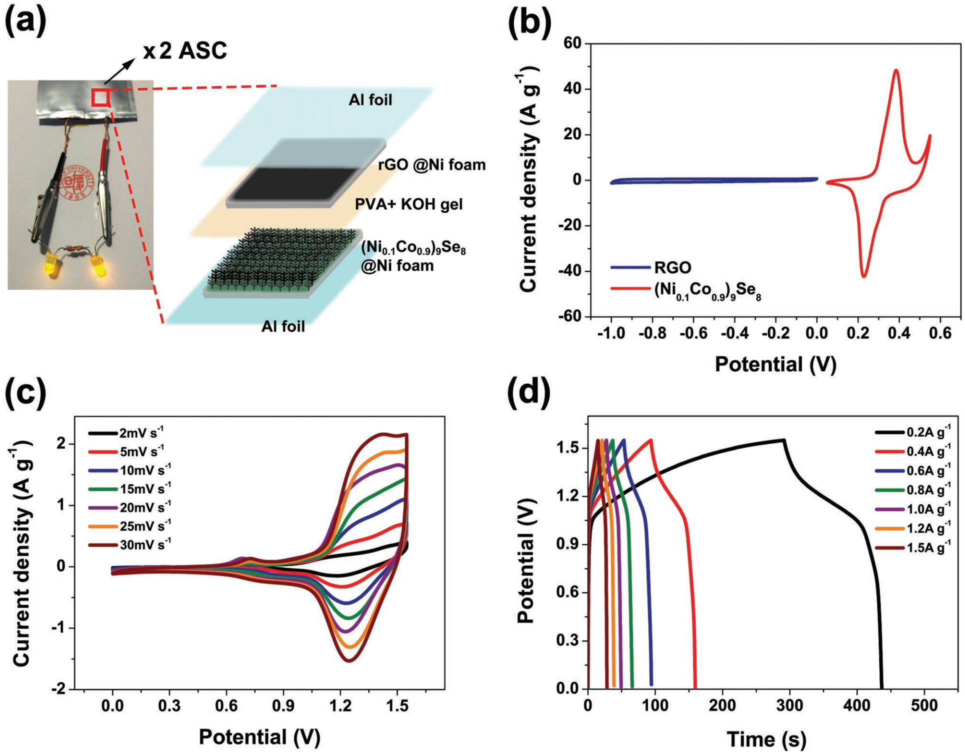

**Figure 4.** a) Photograph (left) and schematic illustration (right) of the light-emitting diode indicators lighted by two $(Ni_{0.1}Co_{0.9})_9Se_8$@NF//PVA/KOH//rGO@NF asymmetric supercapacitors connected in series. b) GCD curves of the as-assembled asymmetric supercapacitor. c) CV curves of the $(Ni_{0.1}Co_{0.9})_9Se_8$ @NF and rGO at a scan rate of 5 mV $s^{-1}$. d) CV curves of the as-assembled asymmetric supercapacitor.

of the device up to 1.55 V. Furthermore, when combined two $(Ni_{0.1}Co_{0.9})_9Se_8$@NF//PVA/KOHgel//rGO@NF ASCs in series, the series-wound ASCs are able to light up two yellow light-emitting diode (LED) light bulbs in tandem connection (≈3.6 V). The CV curves with 0–1.55 V working window at various scan rates are shown in Figure 4c, the well-remained CV curves as scan rate rises to 30 mV $s^{-1}$, indicating the excellent rate capability. Based on the GCD results (Figure 4d), the specific capacitances of the whole asymmetric supercapacitor are calculated to be 27.5, 24.8, 23.2, 22.0, 20.9, 20.4, and 19.8 F $g^{-1}$ at current density of 0.2, 0.4, 0.6, 0.8, 1.0, 1.2, and 1.5 A $g^{-1}$, respectively. Furthermore, the $(Ni_{0.1}Co_{0.9})_9Se_8$@NF//PVA/KOH gel//rGO@NF ASCs exhibits an energy density of 9.1 Wh $kg^{-1}$@225 W $kg^{-1}$ and 6.5 Wh $kg^{-1}$@1751 W $kg^{-1}$, respectively.

With the rising demands of the portable and wearable electrical devices, the optimized $(Ni_{0.1}Co_{0.9})_9Se_8$ nanodendrite arrays are further employed in flexible, foldable energy storage application. Similar to the previous in situ growth strategy, the $(Ni_{0.1}Co_{0.9})_9Se_8$ nanodendrite arrays were grown densely on the CFC substrate. Before the growing, the CFC substrate was pretreated by soaking with a mixture of nitric acid and sulfuric acid to create an uneven surface, which is beneficial for the subsequent in situ growth. The SEM images in **Figure 5**a,b confirm the 3D hierarchical nanodendrite arrays can also be formed in the CFC substrate surface. The CV tests and the corresponding GCD measurements of $(Ni_{0.1}Co_{0.9})_9Se_8$@CFC electrode through three-electrodes configuration are displayed in Figure 5c and Figure S11 (Supporting Information), respectively, revealing a potential window of 0.05–0.55 V and the specific capacitance is calculated to be 591.1 F $g^{-1}$ at current density of 5 A $g^{-1}$. As shown in Figure 5e, the resulting device can be easily folded, pulled, and twisted. The CV and the discharge curves measured at different conditions are presented in Figure 5d,e, respectively. It is obvious that the CV curves at 50 mV $s^{-1}$ remain nearly identical, and the discharge curves at 1 A $g^{-1}$ are similar with a little negative deviation at different states. The long-term durability of the asymmetric supercapacitor can be seen from Figure 5f, which remains 88.8% of its initial capacitance after 3500 cycles. Moreover, two as-assembled $(Ni_{0.1}Co_{0.9})_9Se_8$@CFC//PVA/KOH//GO@CFC foldable ASC connected in series are able to light up a yellow LED light bulb, as seen from the picture in Figure 5g. Accordingly, our $(Ni_{0.1}Co_{0.9})_9Se_8$@CFC//PVA/KOH//rGO@CFC ASC is flexible, mechanically stable which is suitable for wearable devices. The energy density and power density calculated from the GCD data of $(Ni_{0.1}Co_{0.9})_9Se_8$@CFC//PVA/KOH//RGO@CFC ASC is shown in the Ragone plot (Figure 5h). Our device exhibits a high energy density of 17.0 Wh $kg^{-1}$@3.1 kW $kg^{-1}$ and 13.7 Wh $kg^{-1}$@10 kW $kg^{-1}$, respectively. Such high energy density surpasses that of all supercapacitors constructed from nickel-cobalt sulfide and selenide counterpart recently reported.[20,49–60]

In summary, we have successfully developed a one-step, in situ growth of $(Ni_xCo_{1-x})_9Se_8$ solid solution series in various conductive substrates including NF and CFC as advanced electrodes for wearable, asymmetric supercapacitors. Interestingly, the as-grown $(Ni_xCo_{1-x})_9Se_8$ solid solution series spontaneously crystallized into nanodendrite arrays with hierarchical morphology and fractal feature. This unique hierarchical morphology with optimized composition of $(Ni_xCo_{1-x})_9Se_8$ ($x = 0.1$) provides maximized exposed $(01\bar{1})$ surface as well as fast ion diffusion. The resulting $(Ni_{0.1}Co_{0.9})_9Se_8$ nanodendrites deliver a specific capacitance of 3566 F $g^{-1}$ at a current density of 5 A $g^{-1}$ after 5000 cycles. The as-assembled flexible $(Ni_{0.1}Co_{0.9})_9Se_8$@CFC//PVA/KOH//rGO@CFC device exhibits a ultrahigh energy density of 17.0 Wh $kg^{-1}$@3.1 kW $kg^{-1}$ and 13.7 Wh $kg^{-1}$@10 kW $kg^{-1}$, outperforming most recently reported pseudocapacitors based on nickel-cobalt sulfide and selenide counterparts. The resulting solid-state supercapacitor can be easily folded, pulled, and twisted, showing potential application on high-performance wearable and gadget devices. Our study provides rational guidance toward to the design of fractal feature with for superior electrochemical performances due to drastically increased electrochemical active sites. These $(Ni_xCo_{1-x})_9Se_8$ nanodendrites might also be a high-efficiency and robust electrocatalyst for hydrogen evolution reaction (HER) and overall water splitting. Further study of the electrocatalysis properties is still underway.

## Experimental Section

*In Situ Growth of $(Ni_xCo_{1-x})_9Se_8$ Nanodendrite Arrays on Nickel Foam*: The $(Ni_xCo_{1-x})_9Se_8$ nanodendrite arrays were grown on nickel foam by a simple one-step solvothermal method. Prior to the synthesis, nickel foam (10 mm × 35 mm × 0.1 mm) was pretreated with acetone, 2 M HCl solution, deionized water, and absolute ethanol in sequence, each for 15 min, to guarantee a clean surface. The formation of nanodendrites was synthesized via solvothermal route in which benzyl alcohol was used as solvent and with a strictly controlled molar ratio of Co atom and Se atom at 1.2:1. In a typical procedure, 1.0 mmol $SeO_2$ (A.R.), 1.2 mmol $Co(Ac)_2·4H_2O$ (A.R.), and $Ni(Ac)_2·4H_2O$ (A.R.) with different atomic ratios of Co/Ni (0.99/0.01, 0.95/0.05, 0.90/0.10, 0.85/0.15, 0.80/0.20, 0.70/0.30, 0.60/0.40, 0.50/0.50) were added into the solution of benzyl alcohol. After stirring for 1 h, the homogeneous solution was transferred into a 100 mL Teflon autoclave followed by placing a clean piece of nickel foam in it. The autoclave was heated in an oven at 180 °C for 15 h. The final product was washed with ethanol several times and dried in a vacuum oven at 70 °C overnight. The mass loading of the nanodendrite arrays in situ grown on nickel foam was carefully measured for three times to eliminate the possible error.

*Fabrication of rGO/NF Electrodes*: rGO used in the experiment was purchased from Nanjing XF Nanomaterials and Technologies Co. Ltd. (diameter = 0.5–2 µm; thickness ≈ 0.8 nm; monolayer ratio ≈ 80%; purity ≈ 99%) and used directly without any pretreatment. The fabrication process of rGO electrode was as mentioned below: milling a mixture of 72 wt% rGO, 23 wt% acetylene black, 5 wt% of polyvinylidene difluoride and a small amount of ethanol to obtain a well-mixed paste; as-obtained paste then pressed onto a piece of nickel foam to produce rGO electrode.

*Fabrication of $(Ni_xCo_{1-x})_9Se_8$ Nanodendrite/CFC Electrodes*: CFC was purchased from Cetech Co. Ltd. First, a piece of CFC (10 mm × 35 mm × 0.1 mm) was degreased with a solution of acetone, ethanol, and deionized water in 1:1:1 ratio, then soaked with a mixture of nitric acid and sulfuric acid in 1:1 ratio for 30 min to create an uneven surface which is beneficial for the subsequent in situ growth. Afterward, the CFC substrate was rinsed several times with deionized water and ethanol, then dried in a vacuum oven. Similar to the previous in situ growth route, the CFC substrate was immersed into the solution and heated at 180 °C for 15 h. Then the resulting $(Ni_xCo_{1-x})_9Se_8$ nanodendrite/CFC was washed with ethanol and dried in a vacuum oven overnight.

*Fabrication of rGO/CFC Electrodes*: A piece of clean CFC (10 mm × 35 mm × 0.1 mm) was covered with a mixture containing 72 wt% rGO,

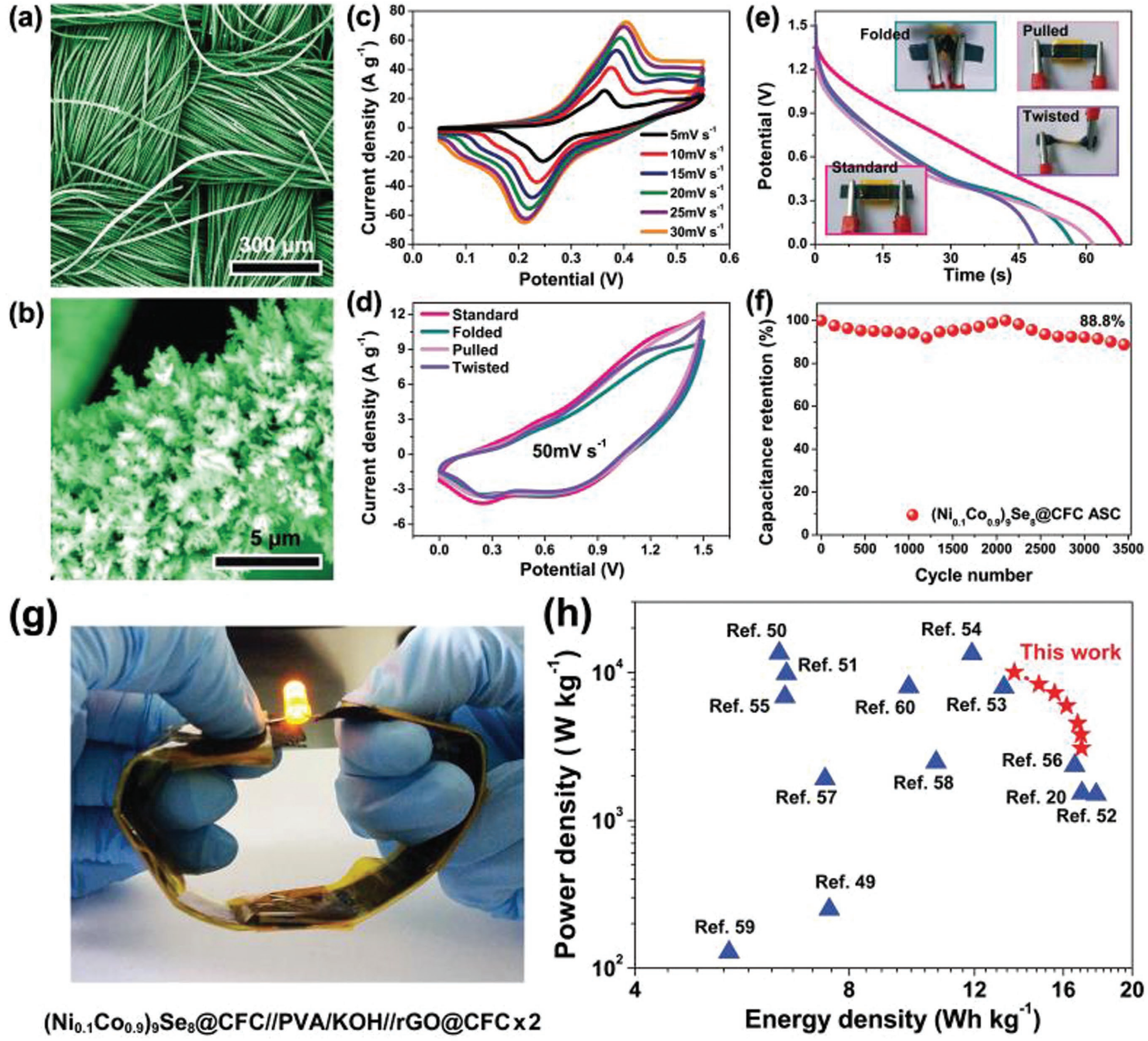

**Figure 5.** a,b) Characteristic SEM images of the as-grown hierarchical $(Ni_{0.1}Co_{0.9})_9Se_8$ nanodendrite arrays on carbon fiber cloth surface. c) CV curves, and d) galvanostatic discharge curves of the $(Ni_{0.1}Co_{0.9})_9Se_8$@CFC. e) CV curves at a scan rate of 5 mV s$^{-1}$, and f) galvanostatic discharge curves at a current density of 1.0 A g$^{-1}$ of the as-assembled flexible asymmetric supercapacitor under different mechanical conditions. g) Photograph of the LED indicator lighted by two $(Ni_{0.1}Co_{0.9})_9Se_8$@CFC//PVA/KOH//rGO@CFC asymmetric supercapacitors connected in series. h) Ragone plot of our work compared with correlative reported supercapacitors based on various nickel-cobalt sulfides and selenides recently reported.

23 wt% acetylene black, 5 wt% of polyvinylidene difluoride, then dried overnight to form a flexible negative electrode.

*Characterization*: The phase structure was characterized by a Bruker D8-A25 diffractometer with Cu Kα radiation. The elemental composition and chemical state of the sample were ascertained by XPS (ThermoFisher Scientific ESCALAB250Xi). SEM (Phenom Pro X) was employed to observe the sample morphologies. TEM and HRTEM images, SAED patterns were obtained from Philips CM 200 FEG field emission microscope. The elemental mapping was performed using JEM-2100F field emission electron microscope.

*Electrochemical Measurement*: The electrochemical characteristic of the $(Ni_xCo_{1-x})_9Se_8$ arrays based on nickel foam or carbon fiber cloth was studied under a three-electrode cell configuration at 25 °C. The nickel foam and carbon fiber cloth supporting as-obtained nanodendrite arrays were soaked in 1 M KOH and acted directly as working electrodes with Ag/AgCl and Pt foil as reference electrode and auxiliary electrode, respectively. The three-electrode cell system was degassed in a vacuum prior to the following measurements. Likewise, the electrochemical properties of the asymmetric $(Ni_{0.1}Co_{0.9})_9Se_8$@NF//PVA/KOH gel//rGO@NF all solid-state supercapacitor and the flexible $(Ni_{0.1}Co_{0.9})_9Se_8$@CFC//PVA/KOH gel//rGO@CFC supercapacitor are further studied under two-electrode cell configuration. Gamry 901 electrochemical workstation (Gamry Instrument Company, USA) was used for electrochemical tests including CV, GCD, and EIS measurements. The EIS measurements were carried out under the factor of the frequency ranges from 0.01 Hz to 100 kHz. To fabricate an asymmetric supercapacitor, the charge balance should follow the relationship $q_+ = q_-$. The charge stored by each electrode ($q$) depends on the specific capacitance ($C$), the potential range for the charge/discharge process ($\Delta E$), and the mass of the electrode ($m$), following the equation: $q = C \times \Delta E \times m$. In order to get $q_+ = q_-$, the mass balancing will follow the equation

$$\frac{m_+}{m_-} = \frac{C_- \times \Delta E_-}{C_+ \times \Delta E_+} \tag{3}$$

The specific capacitances are calculated from the GCD data as the following equation

$$C_\mathrm{s} = \frac{2 i_\mathrm{m} \int V\,\mathrm{d}t}{V^2 \Big|_{V_\mathrm{i}}^{V_\mathrm{f}}} \tag{4}$$

where the $C_\mathrm{s}$ (F g$^{-1}$) is the specific capacitance, current density $i_\mathrm{m} = I/m$ (A g$^{-1}$) with $I$ is the current and the $m$ is mass of the active material, $\int V\,\mathrm{d}t$ is the intergral area of the discharge curve, and the $V$ (V) is the potential with initial and final values of $V_\mathrm{i}$ and $V_\mathrm{f}$, respectively. Similarly, the specific capacitance of the all-solid-state asymmetric supercapacitor is calculated as above, wherein $m'$ (g) is the total mass of active materials from both electrodes.

The energy and power densities are calculated as follows

$$E = \frac{i_\mathrm{m} \int V\,\mathrm{d}t}{3.6} \tag{5}$$

$$P = \frac{E}{\Delta t} \times 3600 \tag{6}$$

where $\Delta t$ (s) is the discharge time.

## Supporting Information

Supporting Information is available from the Wiley Online Library or from the author.

## Acknowledgements

This work was financially supported by the National Natural Science Foundation of China (Nos. 51701042 and 51372040) and Shanghai Rising-Star Program (16QA1400700).

## Conflict of Interest

The authors declare no conflict of interest.

## Keywords

foldable devices, fractal nanodendrites, in situ growth, $(\mathrm{Ni}_x\mathrm{Co}_{1-x})_9\mathrm{Se}_8$, solid solutions

Received: May 8, 2018
Revised: June 8, 2018
Published online: July 15, 2018

---

[1] Y. Huang, M. Zhong, Y. Huang, M. S. Zhu, Z. X. Pei, Z. F. Wang, Q. Xue, X. M. Xie, C. Y. Zhi, *Nat. Commun.* **2015**, *6*, 8.

[2] Y. Huang, M. S. Zhu, Y. Huang, Z. X. Pei, H. F. Li, Z. F. Wang, Q. Xue, C. Y. Zhi, *Adv. Mater.* **2016**, *28*, 8344.

[3] H. F. Li, C. P. Han, Y. Huang, Y. Huang, M. S. Zhu, Z. X. Pei, Q. Xue, Z. F. Wang, Z. X. Liu, Z. J. Tang, Y. K. Wang, F. Y. Kang, B. H. Li, C. Y. Zhi, *Energy Environ. Sci.* **2018**, *11*, 941.

[4] Q. Xue, H. Gan, Y. Huang, M. Zhu, Z. Pei, H. Li, S. Deng, F. Liu, C. Zhi, *Adv. Energy Mater.* **2018**, 1703117.

[5] Y. Huang, M. Zhong, F. K. Shi, X. Y. Liu, Z. J. Tang, Y. K. Wang, Y. Huang, H. Q. Hou, X. M. Xie, C. Y. Zhi, *Angew. Chem., Int. Ed.* **2017**, *56*, 9141.

[6] R. Ma, X. H. Liu, J. B. Liang, Y. Bando, T. Sasaki, *Adv. Mater.* **2014**, *26*, 4173.

[7] P. Simon, Y. Gogotsi, *Nat. Mater.* **2008**, *7*, 845.

[8] K. J. Huang, J. Z. Zhang, J. L. Cai, *Electrochim. Acta* **2015**, *180*, 770.

[9] S. J. Patil, V. C. Lokhande, N. R. Chodankar, C. D. Lokhande, *J. Colloid Interface Sci.* **2016**, *469*, 318.

[10] S. K. Shinde, G. S. Ghodake, D. P. Dubal, R. V. Patel, R. G. Saratale, D. Y. Kim, N. C. Maile, R. R. Koli, H. D. Dhaygude, V. J. Fulari, *J. Taiwan Inst. Chem. Eng.* **2017**, *75*, 271.

[11] S. A. Pawar, D. S. Patil, J. C. Shin, *Mater. Today Chem.* **2017**, *4*, 164.

[12] A. Banerjee, S. Bhatnagar, K. K. Upadhyay, P. Yadav, S. Ogale, *ACS Appl. Mater. Interfaces* **2014**, *6*, 18844.

[13] C. L. Hu, L. Zhang, Z. J. Zhao, A. Li, X. X. Chang, J. L. Gong, *Adv. Mater.* **2018**, *30*, 8.

[14] Z. W. Fang, L. L. Peng, Y. M. Qian, X. Zhang, Y. J. Xie, J. J. Cha, G. H. Yu, *J. Am. Chem. Soc.* **2018**, *140*, 5241.

[15] X. H. Liu, R. Z. Ma, Y. Bando, T. Sasaki, *Adv. Mater.* **2012**, *24*, 2148.

[16] G. Q. Zhang, X. W. Lou, *Adv. Mater.* **2013**, *25*, 976.

[17] X. T. Liang, K. F. Chen, D. F. Xue, *Adv. Energy Mater.* **2018**, 1703329.

[18] H. C. Chen, S. Chen, M. D. Fan, C. Li, D. Chen, G. L. Tian, K. Y. Shu, *J. Mater. Chem. A* **2015**, *3*, 23653.

[19] W. D. An, L. Liu, Y. F. Gao, Y. Liu, J. R. Liu, *RSC Adv.* **2016**, *6*, 75251.

[20] K. L. Guo, S. Z. Cui, H. W. Hou, W. H. Chen, L. W. Mi, *Dalton Trans.* **2016**, *45*, 19458.

[21] P. C. Zhang, L. Chen, T. L. Xu, H. L. Liu, X. L. Liu, J. X. Meng, G. Yang, L. Jiang, S. T. Wang, *Adv. Mater.* **2013**, *25*, 3566.

[22] S. Wang, K. Liu, J. Liu, Z. T.-F. Yu, X. Xu, L. Zhao, T. Lee, E. K. Lee, J. Reiss, Y.-K. Lee, L. W. K. Chung, J. Huang, M. Rettig, D. Seligson, K. N. Duraiswamy, C. K.-F. Shen, H.-R. Tseng, *Angew. Chem., Int. Ed.* **2011**, *50*, 3084.

[23] X. D. Zhang, J. J. Zhang, J. Y. Zhao, B. C. Pan, M. G. Kong, J. Chen, Y. Xie, *J. Am. Chem. Soc.* **2012**, *134*, 11908.

[24] K. Wright, J. D. Gale, *Phys. Rev. B* **2004**, *70*, 8.

[25] L. Vegard, *Z. Phys.* **1921**, *5*, 17.

[26] X. H. Zhong, Y. Y. Feng, W. Knoll, M. Y. Han, *J. Am. Chem. Soc.* **2003**, *125*, 13559.

[27] R. D. Shannon, *Acta Crystallogr., Sect. A* **1976**, *32*, 751.

[28] A. B. Mandale, S. Badrinarayanan, S. K. Date, A. P. B. Sinha, *J. Electron Spectrosc. Relat. Phenom.* **1984**, *33*, 61.

[29] P. Zhang, B. H. Xu, C. X. Gao, G. L. Chen, M. Z. Gao, *ACS Appl. Mater. Interfaces* **2016**, *8*, 30336.

[30] H. Y. Li, D. Gao, X. Cheng, *Electrochim. Acta* **2014**, *138*, 232.

[31] Y. Shao, S. R. Song, X. Wu, J. Qi, H. L. Lu, C. Liu, S. Y. Zhu, Z. L. Liu, J. O. Wang, D. X. Shi, S. X. Du, Y. L. Wang, H. J. Gao, *Appl. Phys. Lett.* **2017**, *111*, 5.

[32] L. Q. Mai, F. Yang, Y. L. Zhao, X. Xu, L. Xu, Y. Z. Luo, *Nat. Commun.* **2011**, *2*, 5.

[33] Y. Cheng, Y. S. Wang, D. Q. Chen, F. Bao, *J. Phys. Chem. B* **2005**, *109*, 794.

[34] D. P. Li, Z. Zheng, Z. Yang, M. Qiang, J. Yu, K. W. Wong, L. Yang, L. Zhi, W. M. Lau, *J. Phys. Chem. C* **2008**, *112*, 2845.

[35] D. P. Li, Z. Zheng, Y. Lei, S. X. Ge, Y. D. Zhang, Y. G. Zhang, K. W. Wong, F. L. Yang, W. M. Lau, *CrystEngComm* **2010**, *12*, 1856.

[36] V. Gupta, S. Gupta, N. Miura, *J. Power Sources* **2008**, *175*, 680.

[37] D. W. Wang, F. Li, M. Liu, G. Q. Lu, H. M. Cheng, *Angew. Chem., Int. Ed.* **2008**, *47*, 373.
[38] Z. J. Fan, J. Yan, T. Wei, L. J. Zhi, G. Q. Ning, T. Y. Li, F. Wei, *Adv. Funct. Mater.* **2011**, *21*, 2366.
[39] R. B. Rakhi, W. Chen, D. Y. Cha, H. N. Alshareef, *Nano Lett.* **2012**, *12*, 2559.
[40] X. Sun, Q. Li, Y. N. Lu, Y. B. Mao, *Chem. Commun.* **2013**, *49*, 4456.
[41] X. H. Xia, Z. Y. Zeng, X. L. Li, Y. Q. Zhang, J. P. Tu, N. C. Fan, H. Zhang, H. J. Fan, *Nanoscale* **2013**, *5*, 6040.
[42] J. P. Liu, J. Jiang, C. W. Cheng, H. X. Li, J. X. Zhang, H. Gong, H. J. Fan, *Adv. Mater.* **2011**, *23*, 2076.
[43] T. Brousse, D. Belanger, J. W. Long, *J. Electrochem. Soc.* **2015**, *162*, A5185.
[44] Y. Gogotsi, R. M. Penner, *ACS Nano* **2018**, *12*, 2081.
[45] P. Simon, Y. Gogotsi, B. Dunn, *Science* **2014**, *343*, 1210.
[46] V. Augustyn, J. Come, M. A. Lowe, J. W. Kim, P.-L. Taberna, S. H. Tolbert, H. D. Abruña, P. Simon, B. Dunn, *Nat. Mater.* **2013**, *12*, 518.
[47] K. Zhu, Q. Wang, J.-H. Kim, A. A. Pesaran, A. J. Frank, *J. Phys. Chem. C* **2012**, *116*, 11895.
[48] Y. Yan, B. Hao, D. Wang, G. Chen, E. Markweg, A. Albrecht, P. Schaaf, *J. Mater. Chem. A* **2013**, *1*, 14507.
[49] Z. H. Wang, Q. Sha, F. W. Zhang, J. Pu, W. Zhang, *CrystEngComm* **2013**, *15*, 5928.
[50] Y. F. Tian, Y. J. Ruan, J. Y. Zhang, Z. X. Yang, J. J. Jiang, C. D. Wang, *Electrochim. Acta* **2017**, *250*, 327.
[51] C. Bo, T. Y. Fan, Y. Z. Xi, R. Y. Jun, J. J. Jun, W. C. Dong, *ChemElectroChem* **2017**, *4*, 3004.
[52] S. A. Ma, S. Q. Zhou, S. L. Wang, M. B. Liu, *J. Alloys Compd.* **2017**, *728*, 592.
[53] H. Peng, G. F. Ma, K. J. Sun, Z. G. Zhang, J. D. Li, X. Z. Zhou, Z. Q. Lei, *J. Power Sources* **2015**, *297*, 351.
[54] G. F. Ma, F. T. Hua, K. J. Sun, E. K. Fenga, H. Peng, Z. G. Zhang, Z. Q. Lei, *R. Soc. Open Sci.* **2018**, 5.
[55] Y. R. Zhu, X. H. Chen, H. Chen, X. B. Ji, Y. Liu, *J. Electrochem. Soc.* **2017**, *164*, A2341.
[56] H. C. Chen, J. J. Jiang, L. Zhang, D. D. Xia, Y. D. Zhao, D. Q. Guo, T. Qi, H. Z. Wan, *J. Power Sources* **2014**, *254*, 249.
[57] C. H. Tang, Z. Tang, H. Gong, *J. Electrochem. Soc.* **2012**, *159*, A651.
[58] W. Kong, C. C. Lu, W. Zhang, J. Pu, Z. H. Wang, *J. Mater. Chem. A* **2015**, *3*, 12452.
[59] M. S. Javed, S. G. Dai, M. J. Wang, D. L. Guo, L. Chen, X. Wang, C. G. Hu, Y. Xi, *J. Power Sources* **2015**, *285*, 63.
[60] Z. B. Wu, X. L. Pu, X. B. Ji, Y. R. Zhu, M. J. Jing, Q. Y. Chen, F. P. Jiao, *Electrochim. Acta* **2015**, *174*, 238.